Chemistry
A European
Journal

Chemistry Europe
European Chemical Societies Publishing

Accepted Article

Title: A reversible hydrogen-bond isomerization triggered by an abrupt spin crossover near room temperature

Authors: Verónica Jornet-Mollá, Carlos Giménez-Saiz, Dmitry S. Yufit, Judith A. K. Howard, and Francisco M. Romero

To be cited as: *Chem. Eur. J.* 10.1002/chem.202003654

Link to VoR: https://doi.org/10.1002/chem.202003654

WILEY-VCH

10.1002/chem.202003654

WILEY-VCH

FULL PAPER

A reversible hydrogen-bond isomerization triggered by an abrupt spin crossover near room temperature

Verónica Jornet-Mollá,[a] Carlos Giménez-Saiz,[a] Dmitry S. Yufit,[b] Judith A. K. Howard,*[b] and Francisco M. Romero*[a]

[a] V. Jornet-Mollá, Prof. Dr. C. Giménez-Saiz, Prof. Dr. F. M. Romero
Instituto de Ciencia Molecular
Universitat de València
P. O. Box 22085, 46071-Valencia, Spain
E-mail: fmrm@uv.es
[b] Dr. D. S. Yufit, Prof. Dr. J. A. K. Howard
Department of Chemistry
Durham University
Durham DH1 3LE, United Kingdom

Supporting information for this article is given via a link at the end of the document.

Abstract: The spin crossover salt $[Fe(bpp)_2](isonicNO)_2 \cdot 2.4H_2O$ (**1**·2.4H_2O) (bpp = 2,6-bis(pyrazol-3-yl)pyridine; isonicNO = isonicotinate N-oxide anion) exhibits a very abrupt spin crossover at $T_{1/2}$ = 274.4 K. This triggers a supramolecular linkage (H-bond) isomerization that responds reversibly towards light irradiation or temperature change. Isotopic effects in the thermomagnetic behaviour reveal the importance of hydrogen bonds in defining the magnetic state. Further, the title compound can be reversibly dehydrated to afford **1**, a material that also exhibits spin crossover coupled to H-bond isomerization, leading to strong kinetic effects in the thermomagnetic properties.

Introduction

The field of molecular bistable materials, in which two different electronic states are selectively accessible under several external stimuli (temperature change, light irradiation, etc.), attracts a widespread interest.[1-7] Spin crossover (SCO) iron(II) complexes are an important class of bistable multifunctional[8-12] materials that can switch between the high spin (HS, S = 2) and low spin (LS, S = 0) states, a process that is associated with a change of optical, magnetic, but also structural properties.[13] For instance, as the complex undergoes crossover from the LS to the HS state a noticeable increase of the Fe^{2+}–ligand bond lengths by ca. 0.2 Å is observed, together with a significant distortion of the octahedral cation environment. In the solid state, this expansion of the Fe^{2+} coordination sphere propagates more or less efficiently throughout the material, depending on the presence of cooperative effects. Often, this results in a nearly isotropic expansion of the crystal lattice. Sometimes, subtle geometrical changes take place along with SCO, involving ligand torsion angles or π-π stacking.[14] These may have a strong impact on the cooperativity of the process. For instance, rotation of methoxyphenyl rings in a heteroleptic bis(terimine) Fe(II) complex leads to partial and gradual SCO showing a wide apparent hysteresis.[15] A very abrupt transformation has been observed in $[FeL_H^{iPr}(SCN)_2]$ (L_H^{iPr} = *N*-2-pyridylmethylene-4-isopropylaniline), where two inequivalent Fe sites undergo simultaneous SCO accompanied by a change of conformation of the isopropyl groups.[16] Also, a complex SCO system with two memory channels related to different conformation of appended butyl groups has been described.[17] Probably the clearest demonstration of the interplay between SCO and ligand movement has been given for Hoffmann clathrates, where it has been shown that a genuine dynamics of rotation of the pyrazine ligands stops in the LS phase.[18]

Anion orientational effects and conformational changes usually entail strongly cooperative processes. Many examples of anion order-disorder transitions showing abrupt and hysteretic SCO are known.[19-22] A special case involves anion displacement with a relative shift of cationic Fe-based layers that leads to an extra stabilization of the LS structure.[23] Less frequent is the study of anion conformational changes. A recent report concerns the iron(III) complex $[Fe(qsal\text{-}I)_2]NTf_2$ (qsal-I = (*N*-8-quinolyl)-5-iodo-salicylaldiminate), in which the triflimide NTf_2^- anion changes from a *syn* conformation in the HS phase to an intermediate conformation in the LS state, resulting in an abrupt SCO taking place near room temperature with a thermal hysteresis of 34 K.[24] Another feature related to cooperativity is the establishment of hydrogen bonding and other intermolecular interactions. In a series of thiophene-functionalized $Fe(phen)_2(SCN)_2$ complexes with the same coordination environment, it has been shown that abruptness is correlated to the presence of weak C–H···S and N–H···S intermolecular contacts in the LS phase that are lacking in the HS phase.[25] Similar examples involving S···S contacts are also known.[26] Particularly interesting in our context is the nitroprusside salt of the $[Fe(bpp)_2]^{2+}$ complex (bpp = 2,6-bis(pyrazol-3-yl)pyridine), which undergoes a very abrupt SCO around T = 182 K. In this salt, the relative orientation of cations and anions changes along the SCO process in order to maintain the hydrogen-bonded network.[27]

In spite of all these related examples, there is a lack of reports concerning drastic rearrangements of the crystal lattice, affecting the connectivity between the Fe(II) complex cations and the anionic sublattice in a reversible manner. We report herein on the complex salt $[Fe(bpp)_2](isonicNO)_2 \cdot 2.4H_2O$ (**1**·2.4H_2O) (isonicNO = isonicotinate N-oxide), exhibiting a phase transition associated to an extremely abrupt SCO process that drives a supramolecular linkage (H-bond) isomerization. The process is relevant due to its exceptional abruptness (the fraction of HS Fe^{2+} cations γ_{HS}

changes from 1 to 0 in less than 3 K at standard cooling rates), its reversibility with respect to temperature change and light irradiation, and its $T_{1/2}$ value close to room temperature.

Photoinduced (and even, thermally induced) reversible supramolecular H-bond isomerizations are rare processes. Usually, this phenomenon is associated to intramolecular H-bonds that respond to the presence of isomerizable moieties, such as azomethines,[28] azo compounds,[29] oximes[30] and hydrazones.[31] Most reports concern solution studies with a few reversible transformations being reported in the solid state.[31] The photoinduced change in the H-bonding pattern of a compound changes its physico-chemical properties and may be of interest in many fields, such as photopharmacology[32] and photoswichable recognition.[33] Further, many biomolecules exhibit this behaviour that can be of interest in the development of optical probes.[34]

Results and Discussion

Synthesis and thermomagnetic properties

Compound **1**·2.4H_2O was synthesised by combining barium isonicotinate N-oxide and *in situ* prepared [Fe(bpp)$_2$]SO_4 in a metathesis reaction. Details of the synthesis and standard characterization are provided in the Experimental Section.

Magnetic susceptibility (χ) measurements of **1**·2.4H_2O were performed in the 2-300 K range (Figure 1a). At room temperature, the product of molar magnetic susceptibility and temperature (χT) equals 3.55-3.77 emu·K·mol^{-1}, in agreement with the expected value for one high-spin Fe^{2+} cation (S = 2 ground state) per formula unit. Upon cooling below 275 K in set mode (average scan rate in the 280-265 K range: 0.054 K·min^{-1}), χT exhibits a stepped decrease in an extremely abrupt manner (inset Figure 1a). The first step ($T_{1\downarrow}$ = 274.6 K) accounts for SCO of a fraction of high-spin Fe^{2+} cations equal to 20%. The remaining iron centres undergo spin crossover in the second step ($T_{2\downarrow}$ = 273.8 K) and the magnetic signal vanishes completely at 273 K. The sample becomes diamagnetic and remains in the S = 0 ground state on cooling further to 2 K. Heating now the sample results in a diamagnetic behavior up to 273 K, where the χT curve shows a sharp increase in a single step ($T_{1/2\uparrow}$ = 274.9 K) to reach the paramagnetic limit at T > 276 K. Asymmetric thermal hysteresis loops are relatively uncommon. Usually, this behaviour has a kinetic origin and it can be due to the presence of hidden phases, multimetastability[35] or other phenomena involving slow dynamics of spin crossover.[36] None of these apply to the present study, which has been made in the quasistatic regime (very slow measurement combined with an almost vertical non-hysteretic transition). Interestingly, Sato and coworkers have shown that a thermodynamic model based on the interaction of three dimeric species (HSHS, HSLS and LSLS) can reproduce these stepped asymmetric hysteresis plots.[37] Although this model is inappropriate in our case due to the complexity of the crystal structure (see below), it is telling us about the importance of intermolecular interactions in this compound.

The magnetic properties point to a first-order phase transition taking place in the 273-276 K temperature range. This was confirmed by differential scanning calorimetry (DSC) measurements. The DSC plot (Figure 1b) obtained upon cooling the sample from 300 K to 200 K shows a sharp exothermic peak located at $T_{\downarrow}$ = 270.7 K. This is significantly lower than $T_{1\downarrow}$ and $T_{2\downarrow}$, and this divergence arises from the different temperature sweeping rates used in the two experiments (10 K·min^{-1} in DSC vs aprox. 0.06 K·min^{-1} in magnetic measurements). Indeed, increasing the sweeping rate in the collection of magnetic data to 0.5 K·min^{-1} (Figure S1) results in a wider thermal hysteresis and a perfect agreement between DSC and magnetic data ($T_{1/2\downarrow}$ = 270.7 K). Enthalpy and entropy changes associated to the phase transition were obtained by integrating the excess heat capacity (after substraction of the lattice contribution) over T and ln$T$, respectively. The calculated values (ΔH = – 14.3 KJ·mol^{-1} and ΔS = – 52.8 J·K^{-1}·mol^{-1}) compare well with those reported for other related complexes showing also very abrupt spin crossover and strong cooperativity.[38-42] The entropy change is much higher than the sum of the electronic part (Rln5 ≈ 13.4 J·K^{-1}·mol^{-1}) and the expected vibronic contribution based on the change of Fe–N distances. This indicates a possible coupling to other intermolecular vibrational modes. On heating the sample back to 300 K, a very sharp endothermic feature is observed at $T_{\uparrow}$ = 274.8 K, with similar values of the thermodynamic parameters (ΔH = 14.7 KJ·mol^{-1} and ΔS = 53.6 J·K^{-1}·mol^{-1}). The excess heat capacity thus mirrors the magnetic behavior and shows the reversibility of the process.

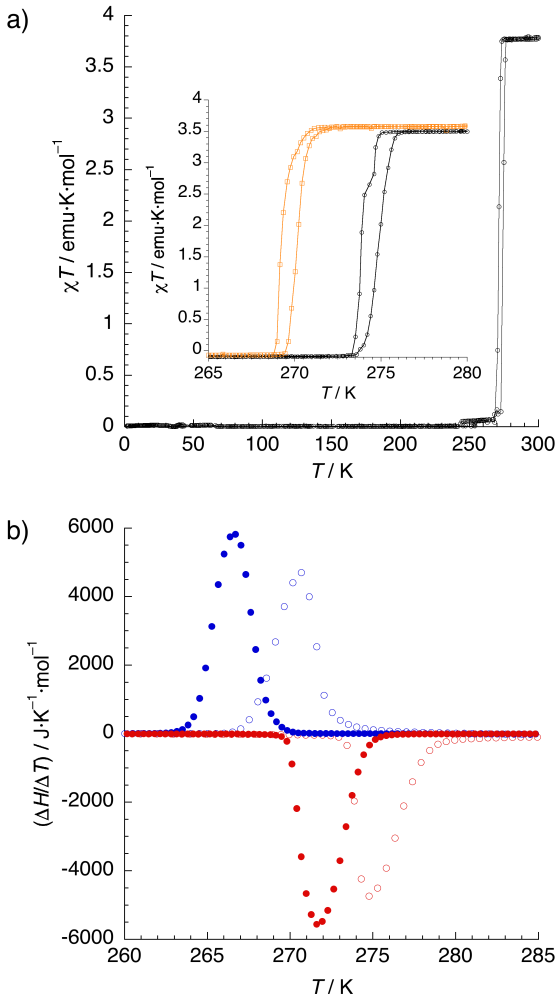

Figure 1. a) Thermal variation of the χT product for **1**·2.4H_2O (temperature scan rate: 1 K·min^{-1}). The inset shows a comparative plot (settle mode) in the spin crossover region of **1**·2.4H_2O (black) and **1**·1.8H_2O·0.6D_2O (orange). b) DSC plot of **1**·2.4H_2O (empty circles) and **1**·1.8H_2O·0.6D_2O (solid circles). Blue and red symbols refer to the cooling and heating modes, respectively.

10.1002/chem.202003654

Photomagnetism

Photomagnetic experiments of **1**·2.4H_2O were conducted in a SQUID magnetometer. The sample was cooled down to 10 K and irradiated at this temperature with a red laser source (λ = 630 nm). The magnetic moment of the initially diamagnetic sample increased with time and reached saturation after an unusally long irradiation time (8 h), when χT = 5.03 emu·K·mol^{-1}, indicating an efficient trapping of the photoinduced high-spin states. Then, irradiation was stopped and the temperature dependence of the susceptibility of **1**·2.4H_2O was measured by heating in the dark at 0.3 K·min^{-1}, following the standard *T*(LIESST) procedure (Figure 2a).[43] After an initial increase, ascribed to ZFS of the quintet ground state, χT reaches a value of 5.25 emu·K·mol^{-1} at 23 K, much higher than that observed at room temperature (3.92 emu·K·mol^{-1}) due to crystal reorientation effects. At temperatures above 40 K, χT decreases sharply and the sample becomes diamagnetic at 66 K indicating a fast relaxation process. The first derivative plot (inset Figure 2a) yields a *T*(LIESST) = 63 K. For $[Fe(bpp)_2]^{2+}$ and similar bischelated iron(II) complexes, *T*(LIESST) can be correlated to the SCO temperature $T_{1/2}$ by the expression *T*(LIESST) = T_0 – 0.3 $T_{1/2}$, where T_0 = 150 K.[44] For $T_{1/2}$ = 1/2($T_{1/2\uparrow}$ + $T_{1/2\downarrow}$)= 274.4 K, a *T*(LIESST) = 68 K should be expected, which is close to the experimental value.

Relaxation measurements were undertaken at different temperatures in the thermally activated regime below 60 K. At the chosen temperature, light was switched off and the time dependence of γ_{HS} was recorded in the dark (Figure 2b). The shape of the different relaxation curves differs from that corresponding to simple first-order kinetics. An initial decrease of around 20% of the signal is observed at the lowest temperatures (54-55 K). Then, the curve becomes sigmoidal, as expected for a strongly cooperative process. In these situations, the rate constant $k^*(T)$ is considered to be dependent on the remaining fraction of HS centres (γ_{HS}) through a self-acceleration factor, $\alpha(T)$, that is a function of temperature. Finally, a residual HS fraction γ_{HS}^{res} has to be considered. The overall behaviour can be reproduced by the following set of equations:

$$\gamma_{HS} = \gamma_{HS}^{res} + 0.2e^{-k_3 t} + (0.8 - \gamma_{HS}^{res})e^{-k^*(T)t} \quad (1)$$

$$k^*(T) = k(T)e^{\alpha(T)(1-\gamma_{HS})} \quad (2)$$

$$k(T) = k(\infty)e^{-E_a/kT} \quad (3)$$

Table 1. Kinetic parameters obtained from relaxation measurements at different temperatures.[a]

T / K	γ_{HS}^{res}	*k* / s^{-1}	α
54	0.147	1.25·10^{-5}	2.85
55	0.088	1.7·10^{-5}	2.80
56	0.144	2.9·10^{-5}	2.75
57	0.107	4.1·10^{-5}	2.70
58	0.095	7.0·10^{-5}	2.65
59	0.096	1.4·10^{-4}	2.60

[a] k_3 = 2.7·10^{-4} s^{-1} was kept constant in the whole temperature range (faster process) to avoid overparametrization.

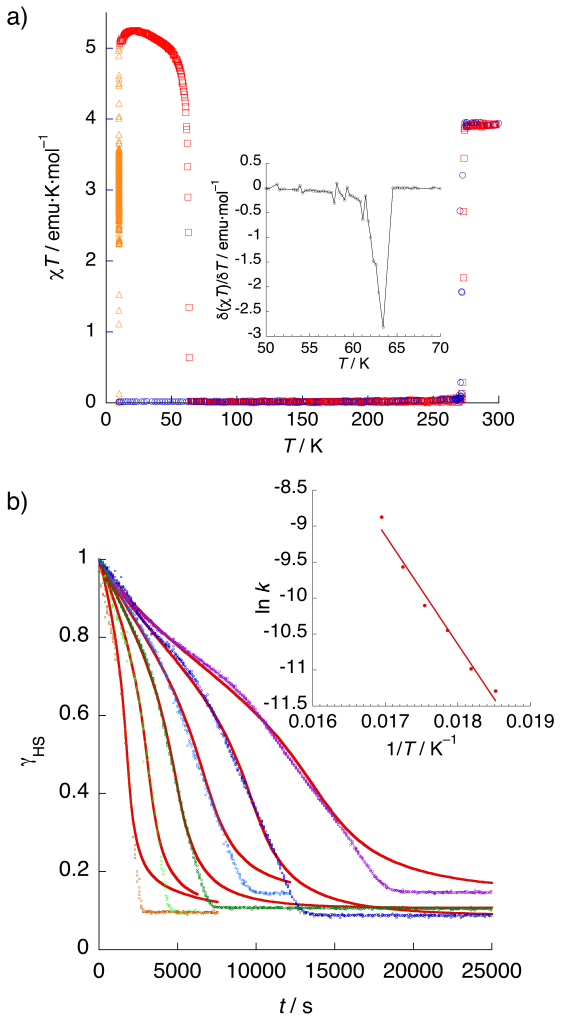

Figure 2. a) Temperature dependence of χT for **1**·2.4H_2O on cooling before irradiation (blue), under irradiation at 10 K (orange) and subsequent heating in the dark at 0.3 K·min^{-1} (red). The inset shows the first derivative of the LIESST plot. b) Time dependence of the high-spin fraction of Fe^{2+} cations at 54 K (purple), 55 K (dark blue), 56 K (light blue), 57 K (green), 58 K (light green) and 59 K (brown). Red lines correspond to the best-fit data according to equation (1). The inset shows an Arrhenius plot corresponding to the thermal variation of the relaxation rate constants, together with the best-fit to Arrhenius equation.

Table 1 gives values of *k* and α at different temperatures, extracted from fitting the relaxation data to the combined equations 1-2. The intrinsic non-cooperative rate constant, *k*(*T*), follows the Arrhenius law (equation 3) (inset Figure 2b) with an apparent activation energy E_a = 1052 cm^{-1}, that lies in the upper range for these compounds. The apparent preexponential factor *k*(∞) is 1.606 × 10^7 s^{-1}. Very high values of α parameter (α > 2.5) were obtained, showing the exceptional cooperativity of the process. The product αT ≈ 107 cm^{-1} remains constant and is a measure of the interaction energy inside the mean-field approximation.[45] Normally, the presence of defects decreases considerably the relaxation rate at low γ_{HS} values, in such a way that the self-accelerated relaxation model overestimates the relaxation rate in these conditions, even for much lower typical α parameters (α < 1). Remarkably, and despite the exceptionally high α values, the relaxation here is faster and much more abrupt than that predicted with self-acceleration. This indicates that,

10.1002/chem.202003654

below a threshold γ_{HS} level, a crystallographic phase transition probably takes place, increasing abruptly the relaxation rate.

Crystal structure analysis

The temperature dependence of the unit cell parameters of **1**·2.4H_2O was first measured by single-crystal X-ray diffraction in the 120-300 K range (Figure S2). Sharp discontinuities were measured for all the parameters between 270 K and 280 K, indicating a crystallographic phase transition in this temperature interval. The change in cell parameters is moderate but anisotropic with Δa = + 0.437 Å (1.9 %), Δb = – 0,164 Å (– 1.2 %), Δc = – 0,039 Å (– 0.14 %). Below the phase transition, the three parameters exhibit positive thermal expansion (mostly inside the *ac* plane with very small variation of the *b* parameter). The temperature dependence of the unit cell volume can be fitted to the linear expression $V(Å^3)$ = 8616.6 + 0.74*T*. This yields a volumetric thermal expansion coefficient for the LS phase α_{LS} = 84×10^{-6} K^{-1}.

1·2.4H_2O crystallizes in the monoclinic *P*2/*c* space group (Table S1). The crystal structure contains three inequivalent Fe^{2+} cations (Fe1, Fe2 and Fe3), each one coordinated to two terdentate bpp ligands that occupy meridional positions of their distorted octahedral FeN_6 coordination spheres. Whereas Fe1 and Fe2 are located in general positions, Fe3 sits on a twofold axis. Each $[Fe(bpp)_2]^{2+}$ complex interacts via π-π stacking with four adjacent complexes to build a two-dimensional lattice (Figure 3a). The structural pattern is similar to the well-known "terpyridine-embrace" motif but in this case the layers are corrugated: stacks of $[Fe(bpp)_2]^{2+}$ units running along the [–101] direction alternate across the average plane of the corrugated layer (Figure S3). There are five independent isonicNO anions (herein denoted by the label of the corresponding NO oxygen atom, see caption to Figure 3) and six H_2O molecules per asymmetric unit that occupy the interlayer space. The carboxylate anions isonicNO(3) and isonicNO(15) stabilize the stacks, as they are both hydrogen-bonded to two adjacent pyrazolyl NH functions in a *syn*, *syn*-bridging mode. Whereas isonicNO(3) (orange) connects Fe1 and Fe3 sites, building symmetric Fe1Fe3Fe1 trimers, isonicNO(15) (purple) bridges Fe1 and Fe2 sites, yielding a dimeric unit. Thus, the combination of the two H-bond interactions defines symmetric pentamers (Figure S4) along the stacks, in which the three Fe sites are connected by strong hydrogen bonds. Two other isonicNO anions are hydrogen-bonded to two $[Fe(bpp)_2]^{2+}$ complexes belonging to different layers (isonicNO(9) (brown) connects Fe1 and Fe3, while isonicNO(6) (magenta) binds Fe1 to Fe2). They act in the same bridging mode, employing both a monodentate carboxylate anion and the N-oxide function (Figure 3b). Finally, isonicNO(12) (light gray) is hydrogen-bonded to the Fe2 site only, the carboxylate function being involved in hydrogen bonding with H_2O molecules.

At 296 K, the Fe–N mean bond distances (2.160 Å, 2.167 Å and 2.162 Å for Fe1, Fe2 and Fe3, respectively) lie in the expected range for an *S* = 2 high-spin (HS) ground state. Octahedral distortion parameters (Table S2) are also typical of HS species,[46] in agreement with magnetic measurements. Below the SCO temperature, the coordination sphere decreases in volume and becomes less distorted. At 120 K, the Fe–N mean bond distances (1.956 Å, 1.959 Å and 1.954 Å for Fe1, Fe2 and Fe3, respectively) indicate that the three Fe^{2+} cations are in the LS state. In comparison to the 296 K structure, the value of the φ parameters approach 180° and Σ decreases considerably, as expected for SCO. The difference between the distortion of the HS and LS phases is less pronounced in the case of Fe3 (located in special positions and representing 20% of the total amount of iron) and this accounts for the faster relaxation process observed in the LIESST experiment.

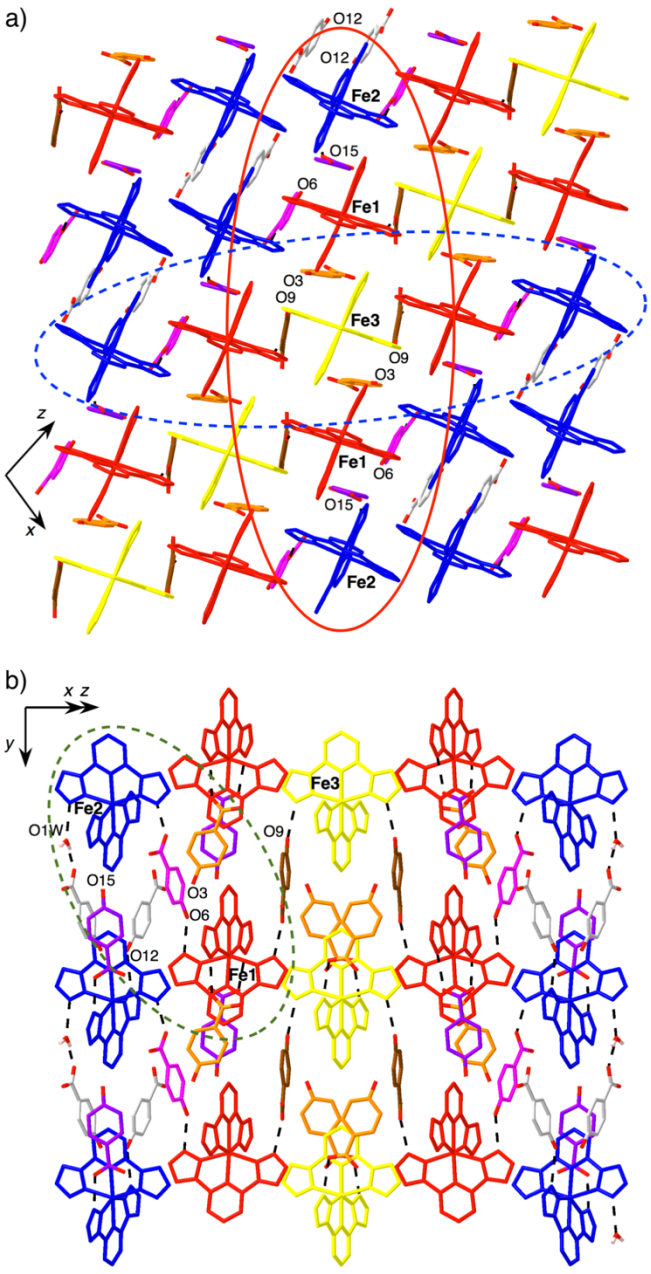

Figure 3. a) View of the X-ray crystal structure (*T* = 296 K, HS phase) of **1**·2.4H_2O along the *b* axis showing the 2D *terpyridine-embrace* motif. The three independent Fe(II) complexes are depicted in different colours: Fe1 (red), Fe2 (blue), Fe3 (yellow). The red oval highlights the presence of pentamers stacked along the [–101] direction. b) A view parallel to the layers, defined by the dashed blue oval in Figure 3a, showing the connectivity between them and emphasizing (dashed green) the presence of isonicNO(6) (magenta) and isonicNO(3) (orange) anions involved in the isomerization process. The remaining anions are depicted in brown (isonicNO(9)), light gray (isonicNO(12)) and purple (isonicNO(15)). Only one water molecule (O1W) is shown.

10.1002/chem.202003654

The abruptness of the phase transition produces a strong rearrangement of the anionic lattice, including the onset of disorder effects at low temperatures. The most striking change concerns the isonicNO(6) anion (magenta): at 296 K (Scheme 1a), its N-oxide function is hydrogen-bonded to a pyrazolyl fragment of the Fe1 site (N1···O6: 2.661(3) Å), while the carboxylate anion binds similarly to the Fe2 site in a monodentate mode (N15···O4: 2.664(3) Å), the other O atom being engaged in a weaker H-bond with a disordered water molecule (O5···O3WA: 2.836(10) Å). This different environment of the O atoms is translated into different C–O distances within the carboxylate unit (C63–O5: 1.231(4) Å; C63–O4: 1.258(4) Å), indicating a polarization of the electron density towards O4, the O atom involved in the stronger H-bond. At 120 K, isonicNO(6) *rotates* by ca. 10° with respect to the cationic lattice (Scheme 1b). It is still bound to the Fe1 site through the NO unit (N1···O6A: 2.603(4) Å) but the N1···O6–N28 bonding angle changes considerably (from 132.8(4)° to 139.8°(3)) upon cooling. The rotational movement of isonicNO(6) breaks the N15···O4 H-bond and brings O5 into a better position to act as a H-bond acceptor (N15···O5A: 2.724(3) Å), keeping the interaction with the water molecule in a bifurcated manner (O5A···O3WA: 2.797(3) Å). This supramolecular linkage (H-bond) isomerization affects the electron density of the carboxylate anion, now strongly polarized towards O5 (C63A–O5A: 1.278(3) Å; C63A–O4A: 1.236(3) Å).

The displacement of isonicNO(6) anions is clearly correlated to the negative thermal expansion observed for the *b* parameter (perpendicular to the cationic layers) across the phase transition. This rotation decreases their tilt angle with respect to the mean plane of the Fe^{2+} cations from 32° (at 280 K) to 24° (at 270 K), thus increasing the interlayer distance.

Another relevant change concerns isonicNO(3) (orange). This anion is connecting adjacent Fe1 and Fe3 sites within the stacks at all temperatures but in the LS phase it establishes with water molecules two weak H-bonding interactions (O3A···O6W: 2.918(3) Å; O2A···O4W: 2.965(4) Å) that are not present in the HS structure (O3···O6W: 3.389(6) Å; O2···O4W: 3.055(4) Å)). A list of hydrogen bond distances found at different temperatures is shown in Table S3.

The combination of π-π stacking interactions plus the H-bonded network connecting the iron sites could be at the origin of the strong cooperativity of the system. Indeed, stacking is reinforced in the LS phase, that keeps the 2D embrace motif but exhibits lower dihedral angles between the neighbouring pyrazolyl mean planes (Table S4). Also, hydrogen bonds are shorter for the LS phase in most cases (Table S3). It is not clear, however, if H-bond isomerism is rather a cause or a consequence of the abrupt phase transition.

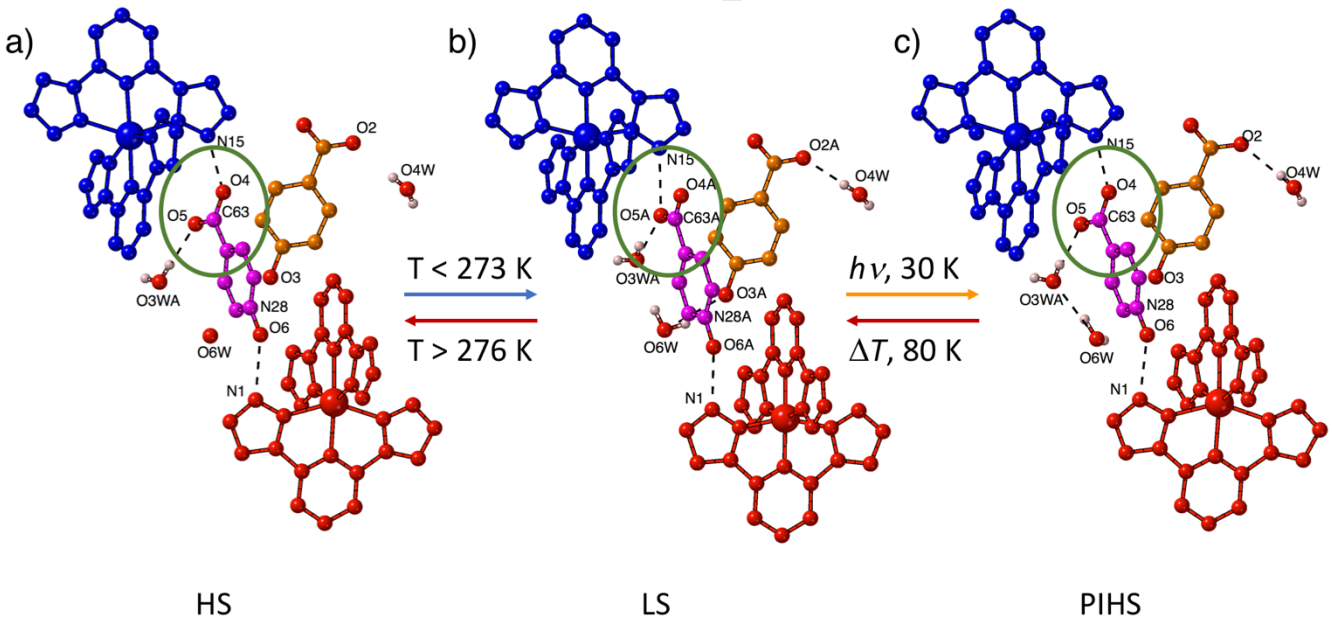

Scheme 1. Reversible supramolecular (H-bond) linkage isomerization coupled to spin crossover (SCO). The material in the HS phase (a) undergoes at T < 270 K SCO to the LS phase (b) with isomerization of the H-bond to isonicNO(6) (magenta) and rearrangement of the H-bonded network involving O3W, O4W and O6W water molecules. These structural changes can be reversed upon heating the LS phase above the SCO temperature or under laser irradiation at 30 K to yield a PIHS phase (c) that relaxes back to the LS phase at higher temperatures. Non-isomerized anions present in the LS phases (occupancy < 0.1) have been omitted.

This question has been elucidated by temperature-dependent X-ray diffraction. The crystal structure of **1**·2.4H_2O was solved at different temperatures below the transition (in the LS phase). In all cases, the atomic coordinates corresponding to the $[Fe(bpp)_2]^{2+}$ cations remain invariant and similar to those observed at 120 K, within the experimental error. Instead, the anionic lattice changes considerably with temperature. At 270 K, the isonicNO(6) anion is split into two positions, A and B, with occupancies of 0.79 and 0.21, respectively (Figure 4a). Position B is very similar to that of the original anion observed in the HS

10.1002/chem.202003654

phase (H-bonded through O4B, Figure S5a), whereas position A matches perfectly that of the isomerized anion present in the 120 K structure (H-bonded through O5A). Interestingly, the occupancy of the B anions decreases upon cooling and becomes less than 0.1 at 120 K (Table 2).

Table 2. Temperature dependence of the occupancy factors of A and B substructures depicted in Figure 4.

T / K	296 (HS)	270 (LS)	260 (LS)	250 (LS)	200 (LS)	120 (LS)	30[a] (HS)	80[b] (LS)
A	nd	0.79	0.82	0.80	0.90	0.92	nd	0.88
B	nd	0.21	0.18	0.20	0.10	0.08	nd	0.12

[a] Photoinduced high-spin (PIHS). [b] Structure obtained after full relaxation of the PIHS phase. nd: no disorder.

A similar behaviour is found in isonicNO(3), also disordered into two positions. In this case, the atomic coordinates of the anion are almost the same in the HS and LS phases and they correspond to the A position (Figure S5b), showing the highest occupancy in the whole temperature range. Instead, the B position, appearing at 270 K and almost vanishing at 120 K, is different from the HS and LS phases (Figure 4b). These results clearly establish that the three relevant structural phenomena (supramolecular linkage (H-bond) isomerization, anion disorder effects and formation of new H-bonds) are subsequent and not prior nor concurrent to SCO.

Isotope effects

The changes in H-bonding connectivity between the HS and LS phases anticipate the observation of isotopic effects[47, 48] in the physical properties of the material and this was confirmed by thermal and magnetic measurements. DSC measurements of a partially deuterated sample **1**·1.8H_2O·0.6D_2O show a similar behaviour to that obtained for the non-deuterated material, with peak maxima shifted to lower temperatures (Figure 1b). Usually, the opposite behaviour is observed.[47] Upon cooling, it shows an exothermic peak at $T_{\downarrow}$ = 266.6 K, while on heating the endothermic peak is observed at $T_{\uparrow}$ = 271.7 K. Note that thermal hysteresis of **1**·2.4H_2O (ΔT = 4.1 K) and **1**·1.8H_2O·0.6D_2O (ΔT = 5.1 K) are similar. Both thermodynamic parameters ΔH and ΔS increase with respect to the non-deuterated compound ($|\Delta H|$ = 16.2 KJ·mol^{-1}; $|\Delta S|$ = 60 J·K^{-1}·mol^{-1}). The isotopic effect is also observed in the magnetic properties (inset Figure 1a) and parallels the thermal behaviour. Again, the SCO temperatures obtained from magnetic data ($T_{1/2\downarrow}$ = 269.2 K; $T_{1/2\uparrow}$ = 270.1 K) differ significantly for those measured by DSC due to the difference in sweeping rates. Thus, in quasistatic conditions, the magnetic behaviour of **1**·2.4H_2O and **1**·1.8H_2O·0.6D_2O is very similar, both compounds showing very abrupt and almost non-hysteretic ($\Delta T \approx$ 1 K) stepped plots (the step is less apparent in the deuterated compound) that are shifted with respect to each other by 4.6 K, evidencing the importance of hydrogen bonds in defining the SCO behaviour. The presence of six inequivalent H_2O molecules and multiple H-bond interaction pathways makes difficult the analysis of the isotope effect in the SCO properties.

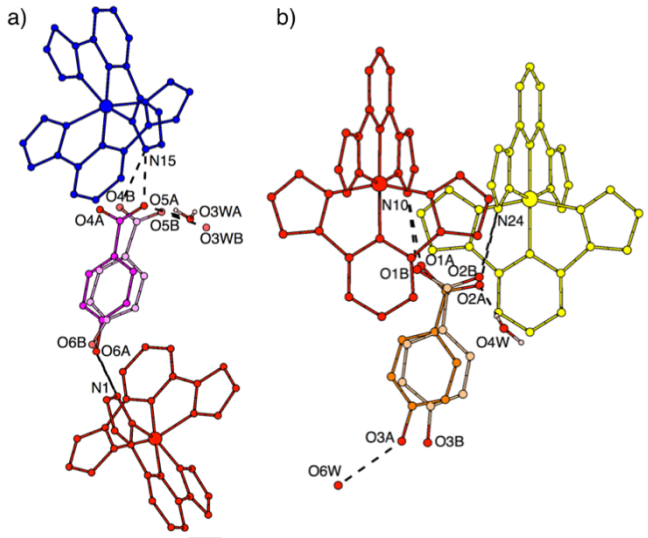

Figure 4. View of the X-ray crystal structure of **1**·2.4H_2O (LS phase) showing the environment of the disordered isonicNO(6) (magenta) (a) and isonicNO(3) (orange) (b) anions. The high and low occupancy fractions of these anions are depicted in dark and light colours, respectively. Occupancies vary with temperature according to Table 2.

Photocrystallography

Photocrystallography experiments were undertaken in order to study the reversibility of these structural changes under light irradiation. Single-crystal X-ray diffraction was performed at 30 K after treatment of **1**·2.4H_2O with a laser source (λ = 630 nm) for 2.5 h. The crystal symmetry is the same (*P*2/*c*) and the crystal cell parameters are close but slightly shorter (Table S1) than those obtained at 296 K, due to thermal contraction. Fe–N distances (mean value of 2.156 Å) and octahedral distortion parameters (Table S2) reveal the trapping of the photoinduced HS state. The structure shows a close match to that obtained at 296 K (Figure S6) with all isonicNO(6) anions binding through O4 and the lack of anion structural disorder. Clearly, the linkage isomerization process has been reversed under light irradiation (Scheme 1c) and this explains the long irradiation time needed for complete excitation. The relative arrangement of adjacent bpp ligands involved in π-π stacking interactions is also reversed, with higher values of dihedral angles (Table S4) and stacking distances more similar but shorter than the HS material (thermal contraction). The H-bond between O3 and O6W is cleaved under light irradiation which, in turn, causes a strengthening of the O6W···O3W interaction. However, the O2···O4W interaction, characteristic of the LS phase, is preserved in the photoinduced material.

The crystal structure of **1**·2.4H_2O was again determined after relaxation of the PIHS at 80 K during 25 min (Table S1). Now the coordination spheres of the three Fe centres (mean Fe–N distance: 1.948 Å, smaller degree of distorsion (Table S2)) indicate complete conversion to the LS state. The structure is very similar to those already described between 270 K and 120 K (Figure S7) with, again, the presence of the isomerized isonicNO(6) anion, the onset of disorder (Table 2) and the formation and cleavage of several H-bonds. All the photoinduced structural changes obtained by LIESST at 30 K are thermally reversed at 80 K.

10.1002/chem.202003654

Magnetic and structural properties of anhydrous 1

One of the most important characteristics of SCO complexes is the memory effect, associated to the presence of a wide thermal hysteresis loop. In principle, removal of the solvent molecules should increase the extent of cation-anion H-bond interactions, hindering the anion reorientation and (if this process is still involved in SCO) leading to a higher thermal hysteresis of kinetic origin. A detailed thermal characterization of the dehydrated compound **1** was thus undertaken. The DSC plot of **1**·2.4H_2O in the 300-400 K range (Figure S8) shows a very intense endothermic peak ($|\Delta H|$ = +126 KJ·mol^{-1}; $|\Delta S|$ = +350 J·K^{-1}·mol^{-1}) that corresponds to the dehydration of the sample. After keeping the sample at 400 K for 2 h, dehydrated **1** was cooled down to 120 K. A very sharp exothermic peak (Figure 5) was observed at $T_{\downarrow anh}$ = 165 K, together with some minor or irreversible features located at higher temperatures (Figure S8). Heating back the sample yields an endothermic peak at $T_{\uparrow anh}$ = 209 K, defining a thermal hysteresis ΔT = 44 K. A second cooling/heating cycle demonstrates that the phase transition is reversible, with only a small shift of the peak maxima (less than 3 K, Figure 5) towards higher temperatures. Mean values of the thermodynamic parameters associated to this phase transition ($|\Delta H|$ = 8.0 KJ·mol^{-1}; $|\Delta S|$ = 43.3 J·K^{-1}·mol^{-1}) are lower than those described for the hydrated compound but still in the range of SCO processes.

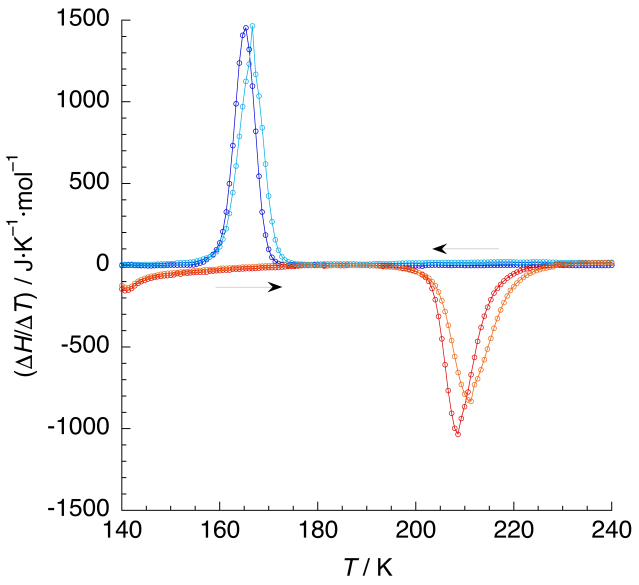

Figure 5. DSC plot for anhydrous **1** in the cooling and heating modes (dark blue and red symbols: first cycle; light blue and orange symbols: second cycle).

The magnetic properties of **1** (Figure 6) were measured after dehydration of the compound *in situ* by thermal treatment at 400 K for 2 h. They are very dependent on the temperature scan rate. The thermal variation of χT measured at 10 K·min^{-1} (same scan rate used in DSC measurements) shows a nearly constant value of 3.6 emu·K·mol^{-1} on cooling from 400 K down to 190 K. Below this temperature, χT decrases abruptly and the sample becomes diamagnetic at 169 K (near $T_{\downarrow anh}$ = 165 K observed in DSC). Upon heating, the diamagnetic behaviour is observed up to 207 K (near $T_{\uparrow anh}$ = 209 K observed in DSC). Then, crossover is observed in two abrupt steps separated by a less steep region around $T_{1/2\uparrow}$ = 257 K. A second cooling/heating cycle (Figure S9a) reveals some new features: a small step appears around 225 K in cooling mode and, remarkably, $T_{1/2\uparrow}$ shifts to higher temperatures (276 K). Normally, a decrease of hysteresis width is observed upon cycling or decreasing the scan rate. In our case, a much larger apparent hysteresis width (ΔT = 95 K) is obtained in the second cycle. Decreasing the scan rate to 2 K·min^{-1} yields a similar trend: now the step is more pronounced and $T_{1/2\uparrow}$ is even higher (293 K). Under these conditions a small residual fraction of HS molecules of about 5% is present at low temperatures.

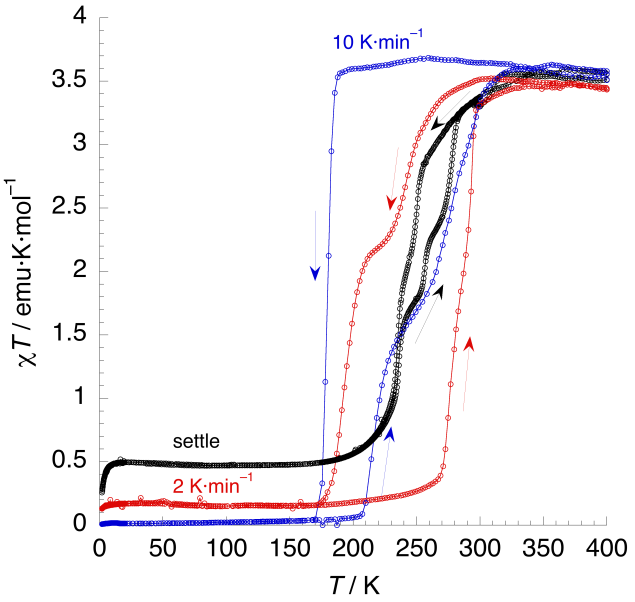

Figure 6. Thermal dependence of χT for anhydrous **1** under different measuring conditions: settle mode (average scan rate: 0.19 K·min^{-1}, black circles) versus sweep mode (2 K·min^{-1}, red circles; 10 K·min^{-1}, blue circles).

The magnetic data are indicative of kinetic effects. Inside the hysteresis loop, relaxation is slow due to the presence of a high activation energy barrier that is likely associated to the structural rearrangement of the H-bonded network that has to take place upon SCO. In these cases, measurements in settle mode at lower scan rates are strongly recommended.[49] The $\chi T = f(T)$ plot measured in settle mode (average scan rate: 0.19 K·min^{-1}) shows a two-step behaviour upon cooling ($T_{1/2\downarrow}$ = 242 K), and a higher residual fraction of HS centers (13%). The heating branch is reversible up to 240 K, then exhibits three steps with increasing hysteretic behaviour (maximum ΔT = 24 K, much less than those observed at higher scan rates). Under these quasistatic conditions, the second cooling/heating cycle (Figure S9b) is quite similar to the first one, with a slightly narrower hysteresis loop as usually observed.

Clearly, in the 300-180 K range of the cooling branch, the HS phase of **1** is metastable. As temperature decreases fast, internal pressure increases until an abrupt and complete HS→LS (probably first-order) transition takes place. Fast heating reverse the phase transition from LS to a mixed-spin state where LS and HS centres are in equilibrium: heating further yields a similar behaviour to that observed in settle mode. When temperature decreases slowly, SCO proceeds more gradually (probably with

no crystallographic phase transition), internal pressure cannot be completely released and a residual fraction of HS molecules is observed. This behaviour is reminiscent of that reported by Real and coworkers, where a kinetically controlled transition between two LS phases toggles the position and width of the hysteresis loop.[17]

Interestingly, the heating branch shows also a metastability range for the LS phase of **1** between 200 and 270 K. As usually observed, except for the first cycle at 10 K·min^{-1}, the scan rate dependence is smaller than for the cooling branch.[50, 51]

The anhydrous compound **1** was structurally characterized in the HS (310 K) and LS (150 K) phases. Although the resolution of the crystal structures is very poor, they can give some insight into the SCO behaviour. Both structures belong to the triclinic *P*–1 space group (Table S5) and are similar to that of the hydrated material, with the 2D arrangement of $[Fe(bpp)_2]^{2+}$ complexes and the isonicNO anions located in between the layers (Scheme 2). In the HS phase, the crystal structure contains a single independent $[Fe(bpp)_2]^{2+}$ complex cation located in a general position, with Fe–N distances lying in the 2.13-2.23 Å range and octahedral distortion parameters characteristic of a HS state (Table S2). A view parallel to the *b* axis shows the layered "terpyridine-embrace" motif in the *ac* plane (Figure S10a), with a strictly parallel arrangement of adjacent pyrazolyl rings along the *c* axis, pointing to stronger π-π stacking interactions. Now the stacks of $[Fe(bpp)_2]^{2+}$ units connected by *syn*, *syn*-bridging isonicNO(3) anions (all of them equivalent and depicted in orange) run along the *a* axis. The two isonicNO anions that are hydrogen-bonded to $[Fe(bpp)_2]^{2+}$ complexes belonging to different layers (isonicNO(6) and isonicNO(9), magenta and brown in Scheme 2a, respectively) are now statically disordered in two positions around an inversion center, averaging the two antiparallel orientations observed in the hydrated compound. This indicates that the hydrogen-bonded network involving the anions rearranges upon loss of water molecules without disrupting the $[Fe(bpp)_2]^{2+}$ layers.

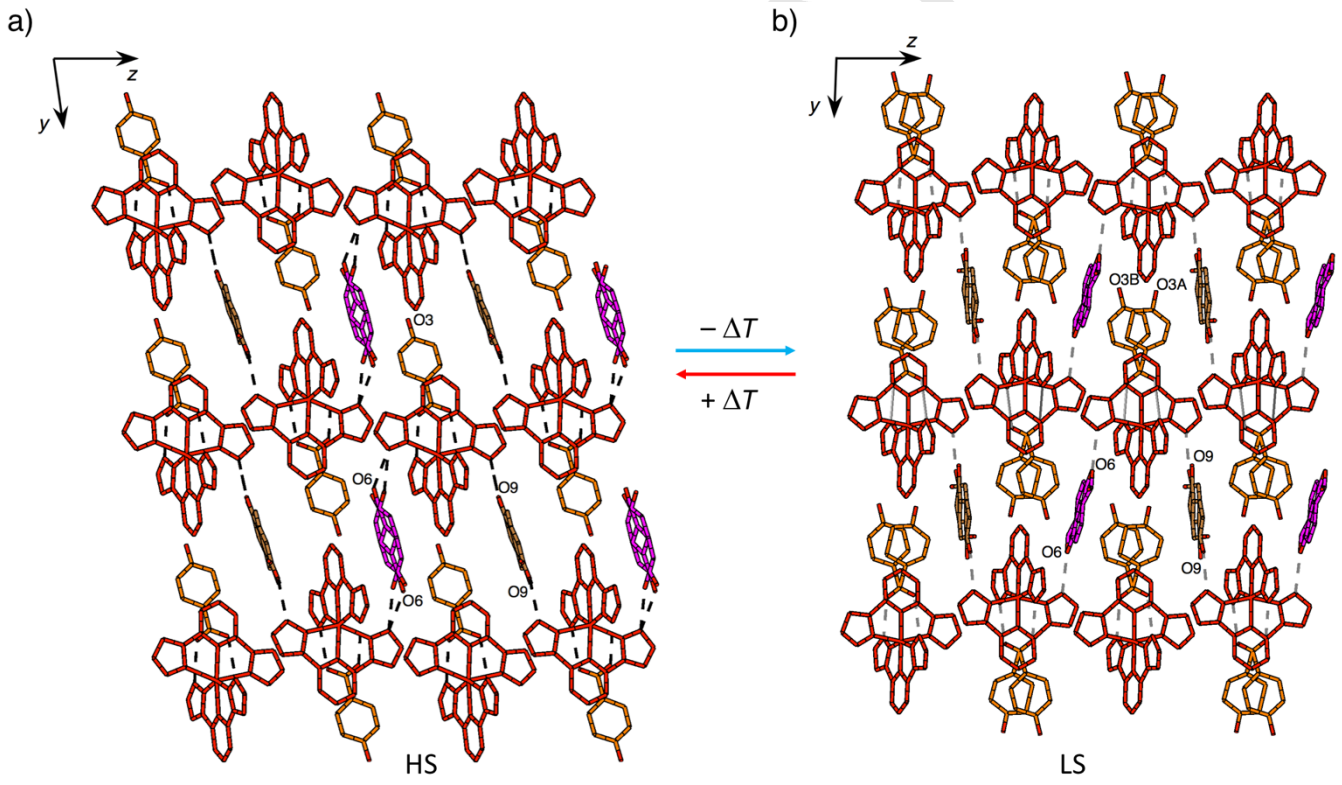

Scheme 2. View along the *a* axis of the crystal structure of anhydrous **1** for both the HS (*T* = 310 K, a) and LS (*T* = 150 K, b) phases, showing the relative shift of the $[Fe(bpp)_2]^{2+}$ layers and the reorientation of the anionic sublattice. IsonicNO(6) (magenta) and isonicNO(9) (brown) are statically disordered around an inversion center in both phases, whereas isonicNO(3) (orange) anions undergo orientational disorder in the LS phase. These structural changes can be reversed upon heating the LS phase above the SCO temperature.

In the LS phase, the unique $[Fe(bpp)_2]^{2+}$ complex cation exhibits Fe–N distances in the 1.94-2.02 Å range and much smaller octahedral distortion parameters (Table S2). The "terpyridine-embrace" layers are maintained (Figure S10b), but now they are shifted with respect to each other along the *c* axis, evidencing a reorientation of the anionic network (Scheme 2). A closer look reveals that the isonicNO(6) anions change their orientation with respect to the cationic layers by as much as 23º (Scheme 3). Also, whereas in the HS phase the inversion center is located within the longitudinal axis of isonicNO(6) anions, in the LS phase it shifts away from this axis. Even if the anionic sublattice is severely disordered, the reorientation is certainly related to a H-bond

isomerization that takes place also in the dehydrated material. The abrupt transformation affects also the isonicNO anions that bridge the $[Fe(bpp)_2]^{2+}$ stacks along the *a* axis, as they become also disordered in two positions (Scheme 2b). The strong rearrangement of the network should involve a high activation energy barrier, explaining the wide metastability range for the HS phase.

Indeed, a variable-temperature PXRD study (Figure S11) shows a constant diffraction pattern upon cooling, that matches the simulated diffractogram for the HS phase, until $T_{\downarrow anh}$ is reached. In contrast, the corresponding metastable LS phase at high temperatures could not be measured in our setup: at temperatures above $T_{\uparrow anh}$, the LS pattern is invariably lost and the HS phase is recovered. This behaviour is consistent with DSC and magnetic measurements at high sweep rates. There is no evidence for the presence of different LS phases that might explain the asymmetry in the hysteresis loop.[17]

Interestingly, the dehydration process is reversible: rehydration yields the original hydrated salt, as confirmed by powder X-ray diffraction and magnetic susceptibility measurements (Figures S12-13).

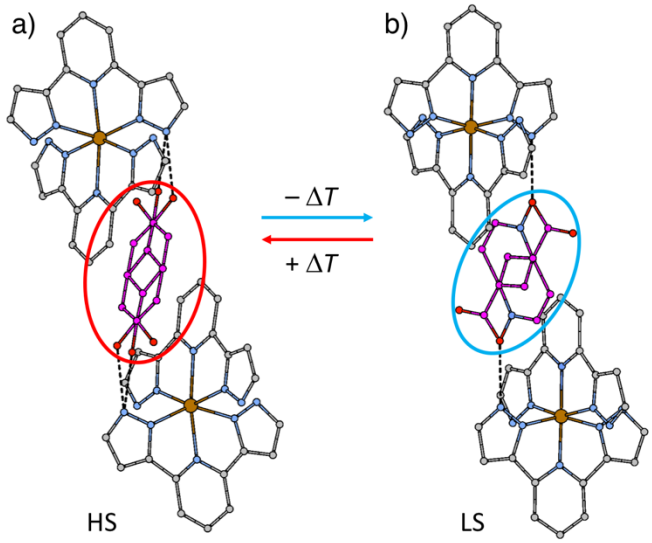

Scheme 3. View of the X-ray crystal structures of anhydrous **1** emphasizing the rotation of isonicNO(6) anions on going from a) the HS phase (T = 310 K) to b) the LS phase (T = 150 K).

Conclusion

In summary, **1**·2.4H_2O exhibits a very abrupt spin crossover, involving three inequivalent Fe^{2+} cations, that triggers a supramolecular linkage (H-bond) isomerization near room temperature. This solid-state transformation can be reversed thermally or under light irradiation. Whereas reversible metal-ligand linkage isomerization processes in transition metal complexes are well studied, with even known examples of coupling to spin crossover,[52, 53] H-bond isomerizations that respond to external stimuli are rare. The study of the crystal structure of **1**·2.4H_2O at different temperatures reveals that anion disorder also results from the acommodation of some anions to the abrupt change of the cationic sublattice. The work shows that the SCO phenomenon can be used to drive reversible structural transformations in solids that are otherwise difficult to achieve. Further, the SCO behaviour related to the isomerization process seems to be present in anhydrous **1**. In this case, the loss of water molecules strengthen the bonding between the $[Fe(bpp)_2]^{2+}$ cations and the isomerizing isonicNO anions, leading to strong kinetic effects in the magnetic behaviour, with the onset of wide hysteresis loops that depend markedly on temperature scan rates. The present work provides also another example[54] of the dependence of SCO on the presence of solvent molecules, a property that can be used in small molecule sensing.

Experimental Section

Synthesis and characterization

Ligand bpp was prepared by the previously published procedure.[55] All other reagents and solvents were used as received.

$Ba(C_6H_4NO_3)_2·4H_2O$

A solution of isonicotinic acid N-oxide (1.046 g, 7.52 mmol) in 40 ml H_2O was combined with a solution of barium hydroxide octahydrate (1.186 g, 3.76 mmol) in 60 ml MeOH. Then, the mixture was refluxed overnight and the resulting solution concentrated using a rotatory evaporator until dryness. The crystalline white product was washed with water and acetone to yield 1.594 g (87 %) of the desired compound. Found: C, 29.42; H, 3.52; N, 5.66. $Ba(C_6H_4NO_3)_2·4H_2O$ requires C, 29.68; H, 3.32; N, 5.77. Thermogravimetric analysis (Figure S14) confirms the presence of four water molecules in this salt. ν_{max}/cm^{-1}: 3394.53, 3108.03, 1598.03, 1545.90, 1390.56, 1225.67, 1177.57, 1139.87, 856.11, 788.13, 685.76, 641.64, 459.14.

*$[Fe(bpp)_2](C_6H_4NO_3)_2·2.4H_2O$ (**1**·2.4H_2O)*

$FeSO_4·7H_2O$ (34.75 mg, 0.125 mmol) was added as a solid to a degassed solution of bpp (53 mg, 0.25 mmol) in 5 ml MeOH yielding a deep red coloured solution after complete dissolution of the metal salt. Then, a solution of $Ba(C_6H_4NO_3)_2·4H_2O$ (206.76 mg, 0.426 mmol) in 5 ml H_2O was added. After stirring for 2 h at room temperature, the off-white precipitate of $BaSO_4$ was filtered through a low-porosity frit. The filtrate was left undisturbed in a thermostatically controlled water bath at 25 °C. Dark orange rhombuses suitable for X-ray analysis appeared after a few days, yielding 44.6 mg (45%). Found: C, 51.02; H, 3.69; N, 20.87. $C_{34}H_{30.8}FeN_{12}O_{8.4}$ requires C, 51.19; H, 3.89; N, 21.07. Thermogravimetric analysis (Figure S15) confirms the presence of 2.4 water molecules in this salt. ν_{max}/cm^{-1}: 3426.63, 3103.77, 1611.42, 1541.58, 1436.44, 1382.85, 1362.58, 1233.40, 782.73, 636.27. A dehydrated sample of **1** for powder X-ray diffraction measurements was obtained by heating *in situ* at 400 K for 2 h. Rehydrated samples of **1** for magnetic and powder X-ray diffraction measurements were obtained by adding two drops of H_2O to the dehydrated material that was left undisturbed for 2 days. The rehydrated compound analyzes as **1**·1.8 H_2O. Found: C, 52.18; H, 3.40; N, 20.95. $C_{34}H_{29.6}FeN_{12}O_{7.8}$ requires C, 51.89; H, 3.79; N, 21.36. This is probably due to partial dehydration of the sample before CHN analysis.

*Deuterated sample (**1**·1.8H_2O·0.6D_2O)*

1·1.8H_2O·0.6D_2O was prepared following the same procedure as described for compound **1**·2.4H_2O, but using deuterated solvents (D_2O and CD_3OD) instead of H_2O and CH_3OH. Elongated orange rhombuses were obtained, yielding 31 mg (31%). ν_{max}/cm^{-1}: 3420.81, 3103.30, 1611.90, 1589.89, 1575.42, 1540.88, 1437.17, 1382.68, 1233.35, 858.29, 782.91, 668.06, 636.97. The fraction of H_2O molecules was calculated as

the ratio of absorbances corresponding to the O–H stretching vibration in the normal and deuterated samples, respectively.

Physical measurements

Variable temperature magnetic susceptibility (χ) measurements were performed using a Quantum Design MPMS-XL-5 magnetometer equipped with a SQUID sensor on polycrystalline samples, applying a magnetic field of 1000 Oe. The pristine, anhydrous and rehydrated materials were first measured in sweep mode. The warming and cooling rates for the original compound were 0.5 K·min^{-1} between 2 and 20 K and 1.0 K·min^{-1} between 20 and 300 K. An additional experiment around the transition temperature (250-280 K) was performed with warming and cooling rates of 0.5 K·min^{-1}. The anhydrous material was obtained by dehydration of the original compound *in situ* in the SQUID equipment at 400 K for 2 h. Then, its magnetic susceptibility was registered at two different sweeping rates (2 K·min^{-1} and 10 K·min^{-1}) in the 400-2 K temperature range (collecting two complete cycles). The rehydrated compound was obtained as described in the *Synthesis and Characterization* section and measured from 250 K to 280 K at 0.5 K·min^{-1}.

Magnetic susceptibility measurements in settle mode were also performed for the original, deuterated and dehydrated samples. Two complete cycles of cooling/warming were acquired for the dehydrated material, instead for the other samples only one complete cycle was registered. The settle mode setting consisted on waiting at each temperature until χ has stabilised within the 5% of tolerance before taking the measurement. For the original compound, the sequence of temperature steps was the following: 2 K (300-290 K), 1 K (290-280 K), 0.20-0.25 K (280-265 K), 1 K (265-260 K) and 2 K (260-250 K). The actual average scan rates in the 280-265 K range were 0.054 and 0.073 K·min^{-1} for the cooling and heating modes, respectively. For the deuterated material, 0.2 and 1 K steps were set in the ranges of 280-265 K and 265-250 K, respectively. This resulted in an average scan rate of 0.08 K·min^{-1} in the hysteresis region (280-265 K). Again, the anhydrous sample was obtained by dehydration of the original compound *in situ* in the SQUID equipment. First, it was heated from 300 K to 400 K at 10 K·min^{-1} (sweep) and kept for 2 h at this temperature. Then, the following sequence was applied: 400-300 K (sweep, at 2 K·min^{-1}), 300-175 K (settle mode, with 0.5 K steps), 175-20 K (sweep, at 2 K·min^{-1}) and 20-2 K (sweep, at 0.20 K·min^{-1}). The averaged cooling/warming rate of the temperature range measured using the settle mode was 0.19 K·min^{-1}.

The photomagnetic measurements were performed by using a thin layer of the compound and a red laser (λ = 630 nm, optical power of 12 mW·cm^{-2}) coupled by means of an optical fiber to the cavity of a Quantum Design MPMS-XL-5 SQUID magnetometer. After cooling to 10 K, the sample was irradiated with red light and the change in magnetization was followed. A fast increase in the signal was observed in 30-35 min, nonetheless, saturation was not reached until 8 h of irradiation. Then, the laser was switched off and the temperature increased at a rate of 0.3 K min^{-1} to determine the T(LIESST) value from the minimum of the $\delta(\chi T)/\delta T$ versus T curve for the relaxation process.

The relaxation kinetics of the metastable high-spin state has been investigated from 54 to 59 K. First, the sample was irradiated at 10 K with a red laser in order to reach the photoinduced high-spin phase. Once saturation of the signal was observed, the sample was warmed while irradiating until the chosen temperature. Then, the laser was switched off and the magnetic susceptibility recorded in the dark as a function of time.

Thermogravimetric (TG) measurements were performed under N_2 atmosphere in a Mettler Toledo TGA/SDTA 851e apparatus in the 298-925 K temperature range at a scan rate of 20 K·min^{-1}.

Differential scanning calorimetry (DSC) analyses were carried out in a Mettler Toledo DSC 821e calorimeter and an automated correction from the sample holder was applied. The temperature sweeping rate was 10 K·min^{-1} and the measurements were undertaken under N_2 atmosphere.

IR spectra were run on KBr pellets using a Nicolet Avatar 320 FT-IR spectrophotometer in the range 4000-400 cm^{-1} at room temperature. CHN elemental analyses were performed in a CE instruments EA 1110 CHNS analyzer.

X-ray diffraction

Suitable crystals of $[Fe(bpp)_2](C_6H_4NO_3)_2{\cdot}2.4H_2O$ (**1**·2.4H_2O) were grown as described in the *Synthesis and Characterization* section and taken from the solution in order to be analyzed. For **1**·2.4H_2O, crystal data were collected on different single-crystals (*a*, *b*, *c*, *d* and *e*) and temperatures: data on samples *a* (296 K), *b* (270, 260 and 250 K) and *c* (80 and 30 K) were collected on a Bruker APEX diffractometer, while data on samples *d* (200 K) and *e* (120 K) were collected on an Oxford Diffraction Supernova diffractometer. Between 296 and 120 K the crystals were cooled in a flow of chilled nitrogen gas by using an Oxford Cryosystems Cryostream.[56] Below 120 K, cooling was carried out in a flow of chilled helium with an Oxford Cryosystems HELIX.[57] Sample *c* was measured first at 30 K after being irradiated during 2.5 h with a red laser (λ = 630 nm, optical power of 5 mW·cm^{-2}), whilst on the diffractometer (these data correspond to the photoinduced high-spin (PIHS) phase at 30 K). After full relaxation, the same sample was measured at 80 K. For the structure determination of anhydrous **1**, two new single-crystals were dehydrated *in situ* at 400 K during 2 h using a stream of hot nitrogen on an Oxford Diffraction Supernova diffractometer. Then, the crystals were cooled in a stream of nitrogen at the working temperature (310 K and 150 K).

The CrysAlis software package[58] was used for the data collection routines, unit cell refinements and data processing of the data acquired in the Oxford Diffraction Supernova diffractometer (equipped with a graphite-monochromated Enhance Mo X-Ray Source, λ = 0.71073 Å). Empirical absorption corrections were performed using the SCALE3 ABSPACK scaling algorithm. On the other hand, the APEX3 software suite[59] was used for data collection, unit cell determination, data reduction, absorption correction, scaling and space group determination of the data collected on a Bruker APEX diffractometer (equipped with a sealed microfocus tube with monochromated Mo Kα radiation, λ = 0.71073 Å). In all cases, the structures were solved with the SHELXT structure solution program[60] and refined on F^2 using full matrix least-squares methods with the SHELXL-2018[61] software, using Olex2.[62]

The structure of **1** is non-merohedrally twinned at both temperatures. The peaks were indexed by using two identical cells with different orientations related by rotation of 180º around the reciprocal *b** axis. The fractional contribution of the minor twinned component refined to 0.483 and 0.497 for the structures at 310 K and 150 K, respectively, using the BASF parameter and the HKLF5 instruction in the SHELXL program integrated in the WINGX program suite.

All non-hydrogen atoms were refined anisotropically, except the atoms of isonicNO(6) and isonicNO(9) anions in the crystal structure of **1** at 310 K and those of all isonicNO anions in the crystal structure of **1** at 150 K. H-atoms bonded to carbon atoms were included at calculated positions and refined as riding atoms with relative isotropic displacement parameters. Instead, H atoms of bpp amino groups and H atoms of water molecules were found in Fourier difference maps, except for the H-atoms of O6W (which were found only in the structures collected at 200 K, 120 K, 80 K and 30 K) and O3WB (the minor component of a disordered water molecule). CCDC1973924, CCDC1973926, CCDC1973928, CCDC1973929, CCDC1973936 and CCDC1973938 contain the supplementary crystallographic data for **1**·2.4 H_2O at 120, 200, 250, 260, 270, and 296 K, respectively. CCDC1973940, CCDC1973941, CCDC1974500 and CCDC2013419 contain the supplementary crystallographic data for the PIHS phase of **1**·2.4 H_2O at 30 K, the LS phase obtained after full relaxation of this PIHS state at 80 K, and the

structure of anhydrous **1** at 310 K and 150 K, respectively. These data are provided free of charge by the Cambridge Crystallographic Data Centre.

Powder X-ray diffraction data were obtained with an Empyrean PANalytical powder diffractometer, using Cu K_α radiation (λ = 1.54056 Å) at room temperature in a 2θ range from 5 to 35°. A 0.5 mm glass capillary was filled with a polycrystalline sample of **1**·2.4H_2O and the dehydrated sample was obtained by heating *in situ* at 400 K for 2 h. The simulated diffractogram was obtained from single crystal X-ray data using the CrystalDiffract software.

Acknowledgements

The present work has been supported by the Spanish MINECO (project CTQ2017-87201-P AEI/FEDER, UE) and Generalitat Valenciana (Prometeo/2019/076 project). V.J.-M. also extends thanks to the MICINN for an FPU fellowship (FPU15/02804). We wish to thank José M. Martínez-Agudo and Gloria Agustí for the magnetic measurements.

Keywords: hydrogen bonds • spin crossover • iron(II) complexes • solvent exchange • isomerization

[1] M. Ruben, K. S. Kumar, *Angew. Chem. Int. Ed.* 10.1002/anie.201911256.
[2] M. S. Alan, M. Stocker, K. Gieb, P. Müller, M. Haryono, K. Student, A. Grohmann, *Angew. Chem. Int. Ed.* **2010**, *49*, 1159.
[3] T. Miyamachi, M. Gruber, V. Davesne, M. Bowen, S. Boukari, L. Joly, F. Scheurer, G. Rogez, T. K. Yamada, P. Ohresser, E. Beaurepaire, W. Wulfhekel, *Nat. Commun.* **2012**, *3*, 938.
[4] A. Holovchenko, J. Dugay, M. Giménez-Marqués, R. Torres-Cavanillas, E. Coronado, H. S. J. van der Zant, *Adv. Mater.* **2016**, *28*, 7228.
[5] Y.-S. Meng, T. Liu, *Acc. Chem. Res.* **2019**, *52,* 1369.
[6] L. Kipgen, M. Bernien, S. Ossinger, F. Nickel, A. J. Britton, L. M. Arruda, H. Naggert, C. Luo, C. Lotze, H. Ryll, F. Radu, E. Schierle, E. Weschke, F. Tuczek, W. Kuch, *Nat. Commun.* **2018**, *9*, 2984.
[7] O. Sato, *Nature Chem.* **2016**, *8*, 644.
[8] J. Y. Ge, Z. Chen, L. Zhang, X. Liang, J. Su, M. Kurmoo, J.-L. Zuo, *Angew. Chem. Int. Ed.* **2019**, *58*, 8789.
[9] M. Darawsheh, L. A. Barrios, O. Roubeau, S. J. Teat, G. Aromí, *Angew. Chem. Int. Ed.* **2018**, *57*, 13509.
[10] H. Zheng, Y.-S. Meng, G. L. Zhou, C.-Y. Duan, O. Sato, S. Hayami, Y. Luo, T. Liu, *Angew. Chem. Int. Ed.* **2018**, *57*, 8468.
[11] S. Ohkoshi, K. Imoto, Y. Tsunobuchi, S. Takano, H. Tokoro, *Nature Chem.* **2011**, *3*, 564.
[12] S. Chorazy, R. Podgajny, K. Nakabayashi, J. Stanek, M. Rams, B. Sieklucka, S. Ohkoshi, *Angew. Chem. Int. Ed.* **2015**, *54*, 5093.
[13] P. Gütlich, H. A. Goodwin in *Spin Crossover in Transition Metal Compounds, Top. Curr. Chem.*, *Vol. 233-235*, Springer Verlag, Berlin-Heidelberg-New York, **2004**.
[14] P. Guionneau, J.-F. Létard, D. S. Yufit, D. Chasseau, G. Bravic, A. E. Goeta, J. A. K. Howard, O. Kahn, *J. Mater. Chem.* **1999**, *9*, 985.
[15] C. Bartual-Murgui, R. Diego, S. Vela, S. J. Teat, O. Roubeau, G. Aromí, *Inorg. Chem.* **2018**, *57*, 11019.
[16] N. Mochida, A. Kimura, T. Ishida, *Magnetochemistry* **2015**, *1*, 17.
[17] M. Seredyuk, M. C. Muñoz, M. Castro, T. Romero-Morcillo, A. B. Gaspar, J. A. Real, *Chem. Eur. J.* **2013**, *19*, 6591; T. Delgado, A. Tissot, L. Guénée, A. Hauser, F. J. Valverde-Muñoz, M. Seredyuk, J. A. Real, S. Pillet, E.-E, Bendeif, C. Besnard, *J. Am. Chem. Soc.* **2018**, *140*, 12870; F. J. Valverde-Muñoz, M. Seredyuk, M. Meneses-Sánchez, M. C. Muñoz, C. Bartual-Murgui, J. A. Real, *Chem. Sci.* **2019**, *10*, 3807.
[18] J. A. Rodríguez-Velamazán, M. A. González, J. A. Real, M. Castro, M. C. Muñoz, A. B. Gaspar, R. Ohtani, M. Ohba, K. Yoneda, Y. Hijikata, N. Yanai, M. Mizuno, H. Ando, S. Kitagawa, *J. Am. Chem. Soc.* **2012**, *134*, 5083.
[19] N. Bréfuel, S. Imatomi, H. Torigoe, H. Hagiwara, S. Shova, J.-F. Meunier, S. Bonhommeau, J.-P. Tuchagues, N. Matsumoto, *Inorg. Chem.* **2006**, *45*, 8126.
[20] G. S. Matouzenko, A. Bousseksou, S. A. Borshch, M. Perrin, S. Zein, L. Salmon, G. Molnár, S. Lecocq, *Inorg. Chem.* **2004**, *43*, 227.
[21] G. A. Craig, J. S. Costa, O. Roubeau, S. J. Teat, G. Aromí, *Chem. Eur. J.* **2011**, *17*, 3120.
[22] T. Fujinami, K. Nishi, D. Hamada, K. Murakami, N. Matsumoto, S. Iijima, M. Kojima, Y. Sunatsuki, *Inorg. Chem.* **2015**, *54*, 7291.
[23] M. Książek, M. Weselski, M. Ilczyszyn, J. Kusz, R. Bronisz, *Chem. Eur. J.* **2019**, *25*, 2250.
[24] N. Phukkaphan, D. L. Cruickshank, K. S. Murray, W. Phonsri, P. Harding, D. J. Harding, *Chem. Commun.* **2017**, *53*, 9801.
[25] Q. Yang, C. Gao, Y.-X. Wang, B.-W. Wang, Z.-M. Wang, S. Gao, *Inorg. Chem.* **2016**, *55*, 7805.
[26] K. Takahashi, T. Kawakami, Z. Gu, Y. Einaga, A. Fujishima, O. Sato, *Chem. Commun.* **2003**, 2374.
[27] K. H. Sugiyarto, W.-A. McHale, D. C. Craig, A. D. Rae, M. L. Scudder, H. A. Goodwin, *Dalton Trans.* **2003**, 2443.
[28] T. Matsuhira, H. Yamamoto, A. Onoda, T. Okamura, N. Ueyama, *Org. Biomol. Chem.* **2006**, *4*, 1338.
[29] E. Procházková, L. Čechová, J. Kind, Z. Janeba, C. M. Thiele, M. Dračinsky, *Chem. Eur. J.* **2018**, *24*, 492.
[30] J.-M. Lehn, *Chem. Eur. J.* **2006**, *12*, 5910.
[31] M. A. Gordillo, M. Soto-Monsalve, C. C. Carmona-Vargas, G. Gutiérrez, R. F. D'vries, J.-M. Lehn, M. N. Chaur, *Chem. Eur. J.* **2017**, *23*, 14872.
[32] J. E. Zweig, T. R. Newhouse, *J. Am. Chem. Soc.* **2017**, *139*, 10956.
[33] Z. Kokan, M. J. Chmielewski, *J. Am. Chem. Soc.* **2018**, *140*, 16010.
[34] K. Brejc, T. K. Sixma, P. A. Kitts, S. R. Kain, R. Y. Tsien, M. Ormö, S. J. Remington, *Proc. Natl. Acad. Sci. USA*, **1997**, *94*, 2306.
[35] M. Nihei, H. Tahira, N. Takahashi, Y. Otake, Y. Yamamura, K. Saito, H. Oshio, *J. Am. Chem. Soc.* **2010**, *132*, 3553.
[36] T. Buchen, P. Gütlich, K. H. Sugiyarto, H. A. Goodwin, *Chem. Eur. J.* **1996**, *2*, 1134.
[37] S. Hayami, Z. Gu, H. Yoshiki, A. Fujishima, O. Sato, *J. Am. Chem. Soc.* **2001**, *123*, 11644.
[38] R. Pritchard, H. Lazar, S. A. Barrett, C. A. Kilner, S. Asthana, C. Carbonera, J.-F. Létard, M. A. Halcrow, *Dalton Trans.* **2009**, 6656.
[39] C. Bartual-Murgui, C. Codina, O. Roubeau, G. Aromí, *Chem. Eur. J.* **2016**, *22*, 12767.
[40] S. Rat, K. Ridier, L. Vendier, G. Molnár, L. Salmon, A. Bousseksou, *CrystEngComm* **2017**, *19*, 3271.
[41] L. Piñeiro-López, F. J. Valverde-Muñoz, M. Seredyuk, C. Bartual-Murgui, M. C. Muñoz, J. A. Real, *Eur. J. Inorg. Chem.* **2018**, 289.
[42] A. Galet, V. Niel, M. C. Muñoz, J. A. Real, *J. Am. Chem. Soc.* **2003**, *125*, 14224.
[43] J.-F. Létard, P. Guionneau, O. Nguyen, J. S. Costa, S. Marcén, G. Chastanet, M. Marchivie, L. Goux-Capes, *Chem. Eur. J.* **2005**, *11*, 4582.
[44] C. Carbonera, J. Sánchez Costa, V. A. Money, J. Elhaïk, J. A. K. Howard, M. A. Halcrow, J.-F. Létard, *Dalton Trans.* **2006**, 3058.
[45] A. Hauser, *Top. Curr. Chem.* **2004**, *234*, 155.
[46] P. Guionneau, M. Marchivie, G. Bravic, J.-F. Létard, D. Chasseau, *Top. Curr. Chem.* **2004**, *234*, 97.
[47] C. P. Köhler, R. Jakobi, E. Meissner, L. Wiehl, H. Spiering, P. Gütlich, *J. Phys. Chem. Solids* **1990**, *51*, 239.
[48] B. Weber, W. Bauer, T. Pfaffeneder, M. M. Dîrtu, D. A. Naik, A. Rotaru, Y. Garcia, *Eur. J. Inorg. Chem.* **2011**, 3193.
[49] S. Brooker, *Chem. Soc. Rev.* **2015**, *44*, 2880.
[50] J.-F. Létard, S. Asthana, H. J. Shepherd, P. Guionneau, A. E. Goeta, N. Suemura, R. Ishikawa, S. Kaizaki, *Chem. Eur. J.* **2012**, *18*, 5924; R. Kulmaczewski, J. Olguín, J. A. Kitchen, H. L. C. Feltham, G. N. L. Jameson, J. L. Tallon, S. Brooker, *J. Am. Chem. Soc.* **2014**, *136*, 878.
[51] A. Bialonska, R. Bronisz, *Inorg. Chem.* **2012**, *51*, 12630.
[52] C.-F. Sheu, C.-H. Shih, K. Sugimoto, B.-M. Cheng, M. Takata, Y. Wang. *Chem. Commun.* **2012**, *48*, 5715.
[53] D. Aguilà, P. Dechambenoit, M. Rouzières, C. Mathonière, R. Clérac, *Chem. Commun.* **2017**, *53*, 11588.
[54] M. C. Giménez-López, M. Clemente-León, C. Giménez-Saiz, *Dalton Trans.* **2018**, *47*, 10453.

10.1002/chem.202003654

[55] Y. Lin, S. A. Lang, *J. Heterocycl. Chem.* **1977**, *14*, 345-347.
[56] Cryostream Cooler, Oxford Cryosystems Ltd, Oxford (UK).
[57] A. E. Goeta, L. K. Thompson, C. L. Sheppard, S. S. Tandon, C. W. Lehmann, J. Cosier, C. Webster, J. A. K. Howard, *Acta Cryst.* **1999**, *C55*, 1243-1246.
[58] CrysAlisPro v38.46, Oxford Diffraction Ltd., 2017.
[59] APEX3 Version 2017.3 (Bruker AXS Inc.)
[60] G. M. Sheldrick, *Acta Cryst.* **2015**, *A71*, 3-8.
[61] G. M. Sheldrick, *Acta Cryst.* **2015**, *C71*, 3-8.
[62] O. V. Dolomanov, L. J. Bourhis, R. J. Gildea, J. A. K. Howard, H. Puschmann, *J. Appl. Cryst*. **2009**, *42*, 339-341.

10.1002/chem.202003654

Entry for the Table of Contents

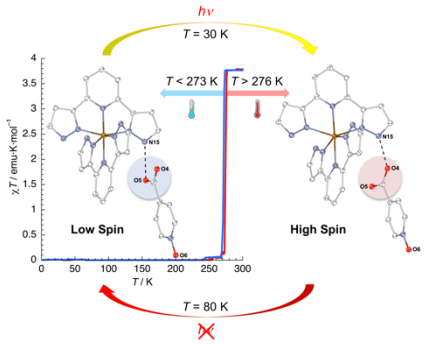

Flip the light on: The iron(II) salt $[Fe(bpp)_2](isonicNO)_2 \cdot 2.4\ H_2O$ (bpp = 2,6-bis(pyrazol-3-yl)pyridine; isonicNO = isonicotinate N-oxide anion) undergoes spin crossover near room temperature ($T_{1/2\uparrow}$ = 274.9 K; $T_{1/2\downarrow}$ = 273.8 K) in an exceptionally abrupt manner (the fraction of HS Fe^{2+} cations γ_{HS} changes from 1 to 0 in less than 3 K). This triggers a hydrogen-bond isomerization in the solid state that can be reversed by temperature change or under light irradiation.